Characterization of the Fe-Doped Mixed-Valent Tunnel Structure Manganese Oxide KOMS-2

Xiongfei Shen,[†] Aimee M. Morey,[‡] Jia Liu,[†] Yunshuang Ding,[†] Jun Cai,[‡] Jason Durand,[‡] Qi Wang,[§] Wen Wen,[||] William A. Hines,[⊥] Jonathan C. Hanson,[||] Jianming Bai,[#] Anatoly I. Frenkel,[§] William Reiff,[$] Mark Aindow,[†] and Steven L. Suib*,[†,‡]

[†]Institute of Materials Science, [‡]Department of Chemistry, and [⊥]Department of Physics, University of Connecticut, Storrs, Connecticut 06269, United States

[§]Department of Physics, Yeshiva University, New York, New York 10016, United States

[||]Department of Chemistry, Brookhaven National Laboratory, Upton, New York 11973, United States

[#]Oak Ridge National Laboratory, Oak Ridge, Tennessee 37831, United States

[$]Department of Chemistry and Chemical Biology, Northeastern University, Boston, Massachusetts 02115, United States

ABSTRACT: A sol−gel-assisted combustion method was used to prepare Fe-doped manganese oxide octahedral molecular sieve (Fe-KOMS-2) materials with the cryptomelane structure. Characterization of the nanopowder samples over a wide range of Fe-doping levels ($0 \leq Fe/Mn \leq 1/2$) was carried out using a variety of experimental techniques. For each sample, Cu Kα XRD and ICP-AES were used to index the cryptomelane structure and determine the elemental composition, respectively. A combination of SEM and TEM images revealed that the

morphology changes from nanoneedle to nanorod after Fe doping. Furthermore, TGA scans indicated that the thermal stability is also enhanced with the doping. Anomalous XRD demonstrated that the Fe ions replace the Mn ions in the cryptomelane structure, particularly in the (211) planes, and results in a lattice expansion along the c axis, parallel to the tunnels. Reasonable fits to EXAFS data were obtained using a model based on the cryptomelane structure. Mössbauer spectra for selected Fe-KOMS-2 samples indicated that the Fe is present as Fe^{3+} in an octahedral environment similar to Mn in the MnO_6 building blocks of KOMS-2. Magnetization measurements detected a small amount of γ-Fe_2O_3 second phase (e.g., 0.6 wt % for the Fe/Mn = 1/10 sample), the vast majority of the Fe being in the structure as Fe^{3+} in the high-spin state.
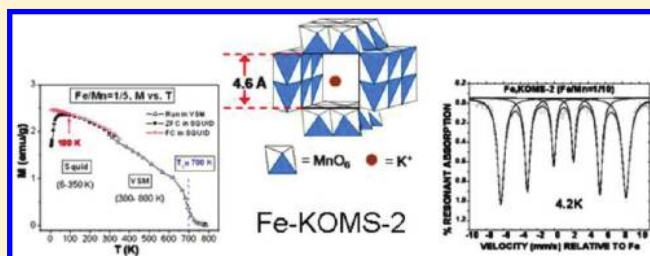
INTRODUCTION

Manganese oxide octahedral molecular sieves (OMS) have been the subject of considerable research activity for several years because of their potential for technological application in catalysis, ion storage and separation, battery electrodes, chemical sensors, and patterning.[1] In addition to their various nanoscale layer and tunnel structures, the manganese oxide OMS have a mixed-valent (Mn) framework, usually +2, +3, and +4, or +3, and +4.[2] Since the Mn ion is capable of a variety of valence states, a variety of magnetic moment values are possible and, therefore, exhibit different types of magnetic behavior. In addition, mixed-valent Mn plays a significant role as a hole carrier, giving rise to a variety of transport properties. Recent reviews of OMS materials and their fabrication, characterization, and applications are available in the literature and online.[3−5]

Among the different OMS materials, KOMS-2 (K_xMnO_2, $x \approx$ 0.1−0.5), a manganese oxide with 2 × 2 tunnel structure, is the most stable form and can be readily synthesized via different methods with the presence of K^+ in the tunnels to provide charge balance and stabilize the structure. The KOMS-2 structure has a rigid MnO_2 framework composed of MnO_6 octahedral building

blocks (see Figure 1a). This one-dimensional square tunnel structure (4.6 Å × 4.6 Å) is formed by double-column walls which are composed of the edge-shared/corner-shared MnO_6 octahedra. The tunnels contain guest cations (in the present case, K^+) which have high mobility due to their weak interaction with the MnO_2 framework. The unit cell of the cryptomelane KOMS-2 structure, which was originally identified by Ramsdell,[6] is tetragonal with $a = b = 9.82$ Å and $c = 2.86$ Å. The manganese ions, which are in the octahedral sites of the cryptomelane KOMS-2 structure, have the Mn^{3+} and Mn^{4+} valence states.[2]

In order to modify the physical and chemical properties of the KOMS-2 system, strategies involving introduction of single-type ions into the tunnels and/or framework have been employed.[7] For example, replacement of some of the K^+ ions by H^+ ions in the KOMS-2 structure has resulted in excellent acid catalysts for selective oxidation reactions.[8] The doping of single-type low- or
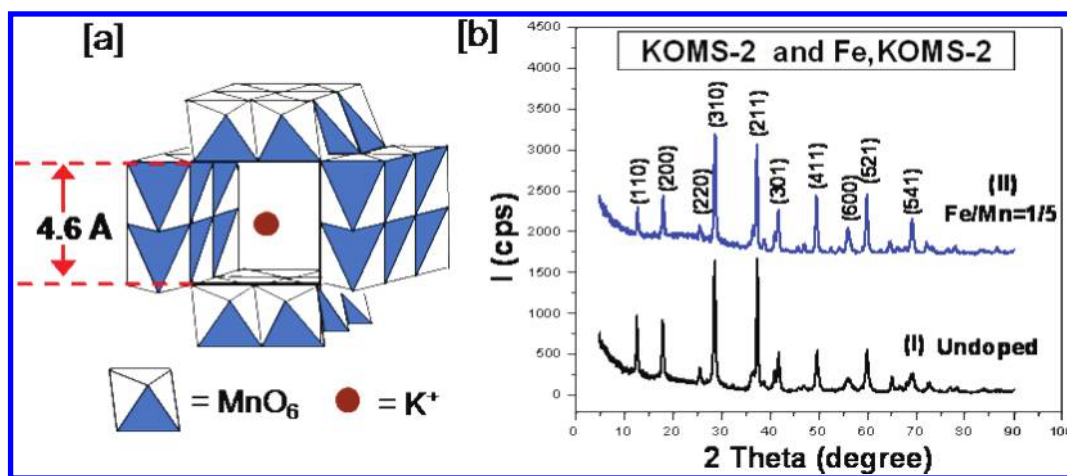
Figure 1. (a) Schematic diagram of the cryptomelane KOMS-2 2 × 2 tunnel structure, which is built up from MnO_6 octahedral units. (b) XRD scans for undoped KOMS-2 and Fe-KOMS-2 (Fe/Mn = 1/5). The cryptomelane structure of KOMS-2 (tetragonal $I4/m$, JCPDS file 29-1020) is maintained for Fe-doping levels up to Fe/Mn = 1/2.

high-valent transition metal ions into the framework has resulted in novel morphologies and catalytic properties.[9]

This work presents a detailed characterization of the Fe-doped KOMS-2 system over a wide range of doping levels $0 \leq$ Fe/Mn $\leq 1/2$. A combination of inductively coupled plasma-atomic emission spectroscopy (ICP-AES), conventional and anomalous X-ray diffraction (XRD), scanning electron microscopy (SEM), transmission electron microscopy (TEM), thermogravanometric analysis (TGA), extended X-ray absorption fine structure (EXAFS) spectroscopy, Mössbauer effect spectroscopy, and magnetometry has been employed to study the morphology, microscopic structure, thermal stability, and magnetic properties. Of particular interest is the location(s) of the doped Fe ions, either in the framework or tunnels or both. The choice of Fe as a dopant is advantageous due to (1) the magnetic properties and (2) Mössbauer effect studies can be applied.

■ EXPERIMENTAL PROCEDURE

A. Sample Synthesis. Nanopowder samples were fabricated by a sol–gel-assisted combustion method.[10] Stochiometric amounts of the nitrate salt precursors KNO_3, $Mn(NO_3) \cdot 4H_2O$, and $Fe(NO_3)_3 \cdot 9H_2O$ were dissolved in distilled water along with the cross-linking agent glycerol. Samples were prepared with nominal Fe/Mn atomic ratios = 1/20, 1/10, 1/5, 1/3, and 1/2. The resulting solution was heated at approximately 100 °C to form a gel by evaporating the water. The dry gel was then transferred to an oven for combustion in air at 250 °C for 2 h resulting in a black powder. The powder was then calcined at 600–800 °C in air to form the final Fe-KOMS-2 product. Additional details can be found in ref 10. For comparison, an undoped KOMS-2 sample was prepared without the Fe nitrate salt precursor using the same combustion/calcination procedure. The elemental composition for all of the KOMS-2 and Fe-KOMS-2 samples was determined by ICP-AES using a Perkin-Elmer model 140 instrument. Table 1 lists the nominal Fe/Mn atomic ratios and measured elemental compositions for the samples studied in this work.

Conventional powder XRD analysis was carried out on all of the samples using a Scintag PDS 2000 diffractometer with Cu Kα radiation (λ = 1.54185 Å) in the step scan mode with a scan rate

Table 1. Fe-Doped KOMS-2 Samples

sample no.	Fe/Mn (molar)	Fe % (wt. %)	formula
1	0	0	$K_{0.13}MnO_2$ (undoped KOMS-2)
2	1/10	5%	$K_{0.16}(Fe_{0.10}Mn_{0.92})O_2$
3	1/5	10%	$K_{0.20}(Fe_{0.16}Mn_{0.85})O_2$
4	1/3	17%	$K_{0.27}(Fe_{0.26}Mn_{0.80})O_2$
5	1/2	20%	$K_{0.30}(Fe_{0.32}Mn_{0.76})O_2$

of 2 s/step and a step size of 0.01° (2θ). All of the Fe-KOMS-2 samples show the same cryptomelane structure (JCPDS file 29-1020) as KOMS-2. The pure cyptomelane phase is tetragonal with space group $I4/m$ and unit cell parameters $a = b = 9.82$ Å and $c = 2.86$ Å, where the c axis is parallel to the tunnels. Figure 1a shows a schematic picture of the 2 × 2 tunnel cryptomelane structure of KOMS-2 which is composed of MnO_6 octahedral building blocks. A representative XRD scan with indices for the Fe-KOMS-2, Fe/Mn = 1/5, sample along with that for undoped KOMS-2 are shown in Figure 1b. Fe/Mn = 1/2 was the maximum Fe-doping level achieved in this work while maintaining the host cryptomelane structure. Although conventional XRD scans show only a single-phase cryptomelane structure, a trace amount of γ-Fe_2O_3 (maghemite) second phase was present (see below).

B. Materials Characterization. The initial structural analysis of each sample was performed by conventional powder XRD, while the elemental composition was determined by a combination of ICP-AES spectroscopy and AOS titrations. In addition, the morphology of the materials was observed with a Zeiss DSM 982 Gemini field emission (SEM). Powder specimens were dispersed in acetone, dropped onto a gold-coated silicon wafer, and then dried. The wafer was mounted onto a stainless steel sample holder. The microstructure of the materials was studied by high-resolution TEM using a JEOL 2010 FasTEM operating at 200 kV. The instrument is equipped with a high-resolution objective lens pole-piece (Cs = 0.5 mm) giving a point-to-point resolution of <0.19 nm in phase contrast images. The sample powder was dispersed in propanol and dropped onto a carbon-coated 300 mesh copper grid, where the propanol was allowed to evaporate. Thermogravimetric analysis of the stability for the materials was carried
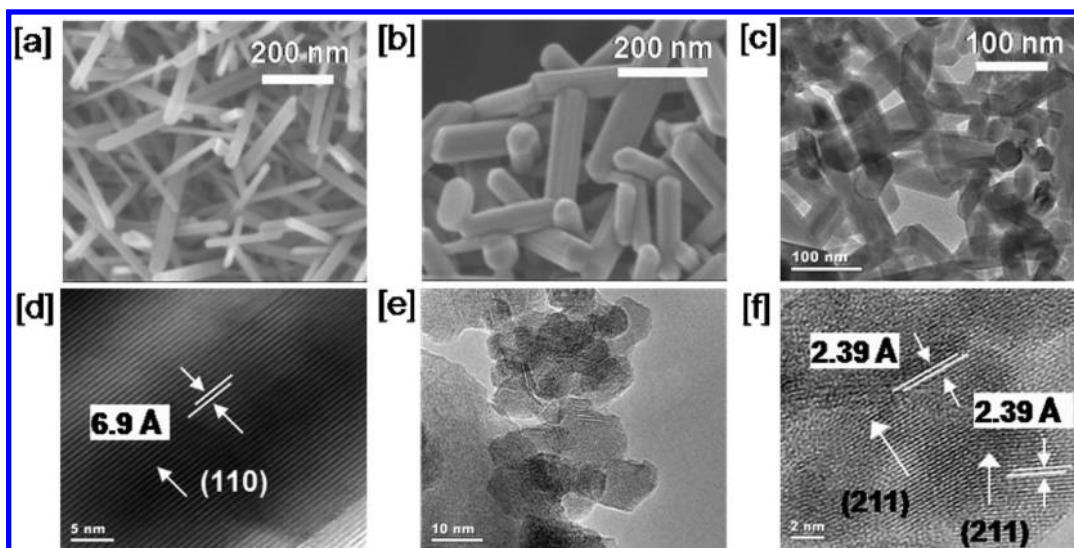
Figure 2. Scanning electron microscopy images of (a) undoped KOMS-2 and (b) Fe-KOMS-2 (Fe/Mn = 1/5). The needle-like morphology (diameters 30–40 nm) of KOMS-2 is transformed to a rod-like morphology (diameters 80–100 nm) after Fe doping. Transmission electron microscopy images of Fe-KOMS-2 (Fe/Mn = 1/5) provided information concerning the microstructure. (c) Nanorod morphology is maintained for shorter ultrasonic pretreatment times. (d) The 6.9 Å distance between the fringes corresponds to the d spacing of the (110) lattice planes for the tetragonal cryptomelane KOMS-2 structure. (e) Some small particles, with diameters 10–20 nm, are observed for longer ultrasonic pretreatment time (10–30 min). (f) The 2.39 Å distance between the fringes for the small particles corresponds to the d spacing of the (211) lattice planes for the tetragonal cryptomelane KOMS-2 structure.

out from 25 to 700 °C at a heating rate of 20 °C/min on a Hi-Res TGA model 2950 system using a 60 mL/min N_2 flow atmosphere. Mössbauer spectra were obtained using a conventional constant acceleration spectrometer operated in the multiscaling mode with a γ-ray source of ^{57}Co in a rhodium metal matrix. The spectrometer was calibrated with a 6 μm thick natural abundance iron foil. Anomalous XRD and EXAFS data were collected at the National Synchrotron Light Source at Brookhaven National Laboratory utilizing beamlines X7B, X11A, X14A, and X23B2. Magnetic measurements were carried out over a temperature range 6 K ≤ T ≤ 800 K and for magnetic fields $|H|$ ≤ 50 kOe using a combination of a Quantum Design MPMS SQUID magnetometer and a Princton Applied Research model 155 vibrating sample magnetometer (VSM).

■ RESULTS AND ANALYSIS

A. Electron Microscopy. Scanning electron microscopy was used to study the morphology of the materials. Figure 2a shows the nanoneedle-like morphology for undoped KOMS-2 with diameters ranging from 30 to 40 nm. After Fe doping, KOMS-2 changes its morphology from nanoneedle shape to nanorod shape (80–100 nm in diameter) as shown for Fe-KOMS-2, Fe/Mn = 1/5, in Figure 2b. The SEM images show a uniform morphology for both undoped and Fe-doped KOMS-2. The microstructure of nanoscale Fe-KOMS-2 was studied by TEM. As shown in Figure 2c and 2d for Fe-KOMS-2, Fe/Mn = 1/5, the TEM images confirm that the nanorods of Fe-KOMS-2 have the KOMS-2 cryptomelane structure as indicated by the lattice fringes. The 6.9 Å distance between the fringes in Figure 2d corresponds to the d spacing of the (110) lattice planes. Some small particles, with diameters ranging from 10 to 20 nm, can also be observed after longer times of ultrasonic pretreatment (10–30 min) as shown in Figure 2e and 2f. Measurements of the lattice fringes indicate that these particles also have the KOMS-2 structure. The

lattice fringes shown for these particles have a spacing of 2.39 Å, which corresponds to the (211) planes (see Figure 2f). The Fe-KOMS-2 crystals have different orientations (polycrystalline). No such small particles were observed when the ultrasonic pretreatment time was less than 10 min. Even for the longer pretreatment times, only a very few regions in the TEM images showed the presence of these small particles. Finally, the TEM results for Fe-KOMS-2 indicate that only the cryptomelane structure is present; no other phases, such as trace amounts of γ-Fe$_2$O$_3$, are observed.

B. Thermal Analysis. The thermal stability of the materials was analyzed by TGA measurements in an N_2 atmosphere. As illustrated in Figure 3a, all of the samples only show a major weight loss (>6 wt %) for temperatures greater than 600 °C. This weight loss is associated with the release of oxygen in the structure causing a structural collapse as seen in other OMS materials.[11] The differentiated TGA curves are shown in Figure 3b. The structural collapse temperature increases with Fe doping in Fe-KOMS-2. For Fe/Mn = 0, 1/20, 1/10, 1/5, and 1/3, the structural collapse temperatures are 750, 756, 766, 777, and 784 °C, respectively. The TGA scans for undoped KOMS-2 and the Fe-KOMS-2 materials did not show any extra weight loss peaks which could be assigned to other phases.

C. Anomalous X-ray Diffraction. Anomalous XRD was used to determine if Fe replaces Mn in the KOMS-2 structure by comparing XRD data at different energies, i.e., the Mn edge, the Fe edge, and an energy far away from the Mn and Fe edges. Since the absorption edge for an element in a compound is generally different from that in the zero oxidation state (metal), preliminary direct measurements of the Mn and Fe absorption edges were made for Fe-KOMS-2, Fe/Mn = 1/5. Values of 6550 and 7112 eV were obtained for the Mn and Fe absorption edges, respectively. (The corresponding zero oxidation state values are 6539 and 7113 eV, respectively.) An X-ray energy of 16 keV was used as an energy far away from the Mn and Fe edges. For comparison, the Cu Kα energy is 8042 eV.
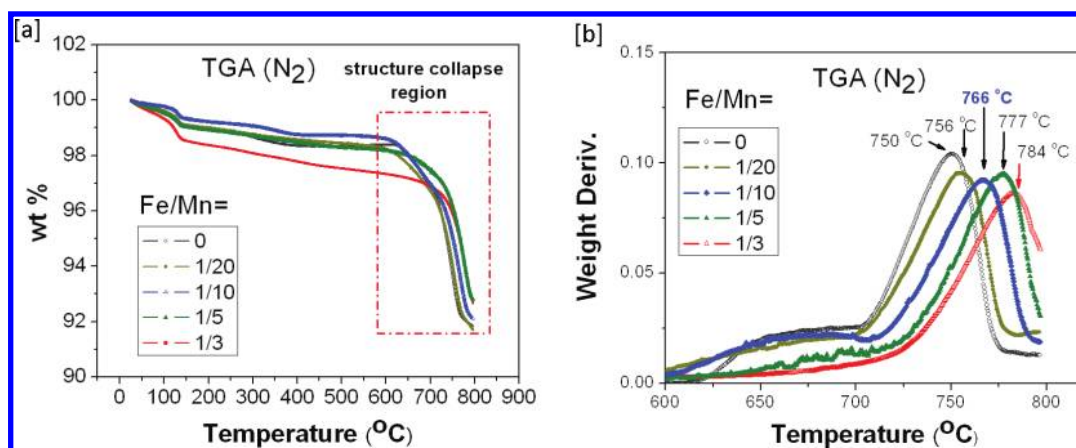
Figure 3. (a) As-measured TGA profiles, weight loss versus temperature, for undoped KOMS-2 and Fe-KOMS-2 for various Fe-doping levels. (b) Derivative TGA profiles yielding thermal stability temperatures for undoped KOMS-2 and Fe-KOMS-2 materials. The structural collapse temperature, which is associated with release of oxygen from the structure, increases with increasing Fe doping.
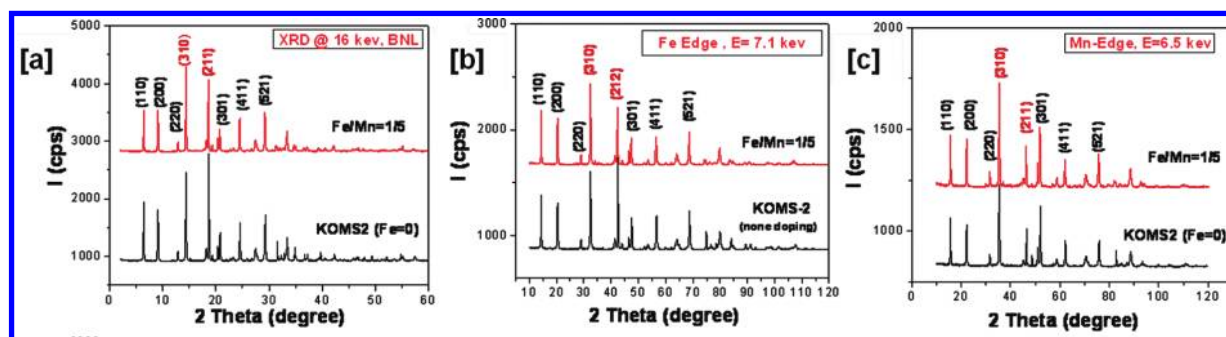

Figure 4. X-ray diffraction scans for the Fe-KMS-2 (Fe/Mn = 1/5) sample obtained with X-ray energies: (a) 16 (far away), (b) 7.1 (Fe edge), and (c) 6.5 keV (Mn edge). For the three energies, Fe-KOMS-2 can be indexed on the tetragonal cryptomelane structure when Fe/Mn $\leq$ 1/2; however, the intensities of some peaks change with the radiation energy.

Figure 4a, 4b, and 4c shows the XRD scans obtained for Fe-KMS-2, Fe/Mn = 1/5, with energies of 16 (far away), 7.1 (Fe edge), and 6.5 keV (Mn edge), respectively. Fe-doped KOMS-2 can be indexed on the tetragonal cryptomelane structure for Fe/Mn $\leq$ 1/2, and this is the case for the three energies illustrated in Figure 4. However, the intensities of some peaks clearly change with the radiation energy, in particular, the peak intensity for the (211) reflection relative to the (310) reflection (I_{211}/I_{310}). Figure 5 shows the dependence of the intensity ratio I_{211}/I_{310} on the Fe-doping level in Fe-KOMS-2 for the three X-ray energies, 6.5, 7.1, and 16 keV. For the undoped KOMS-2 sample, the ratio I_{211}/I_{310} is the same for 16 (far away) and 7.1 keV (Fe edge); however, the ratio decreases dramatically for 6.5 keV (Mn edge). In general, I_{211}/I_{310} decreases with increasing Fe-doping levels from Fe/Mn = 0 to 1/2 for all three energies as shown in Figure 5. However, I_{211}/I_{310} shows a more rapid rate of decrease, at least initially, for the data obtained at 16 and 7.1 keV compared to that for 6.5 keV (Mn edge, where the Mn is suppressed). This indicates that there are decreasing amounts of Mn atoms in the (211) planes with increasing Fe-doping levels, i.e., Mn ions in the (211) planes are being replaced by Fe ions.

In addition to the changes in peak intensity with Fe doping, changes in the positions of some peaks were also observed. Figure 6a and 6b shows detailed XRD scans obtained at 16 keV over the ranges $6° \leq 2\theta \leq 16°$ and $18° \leq 2\theta \leq 25°$, respectively, for undoped KOMS-2 and Fe-KOMS-2, Fe/Mn = 1/5. As seen in
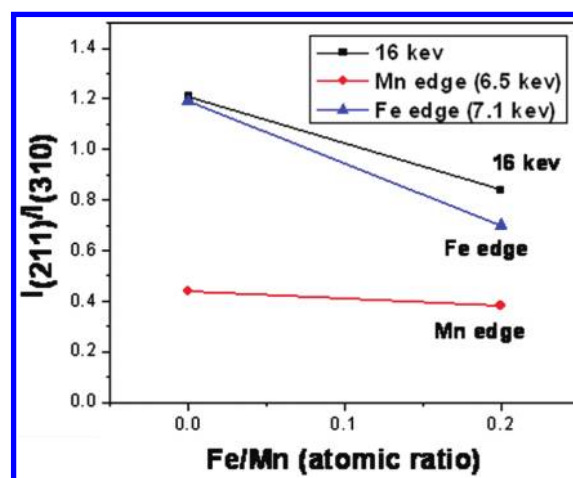

Figure 5. Intensity ratio of the (211) to (310) peaks, I_{211}/I_{310}, versus the Fe-doping level in Fe-KOMS-2 for the three X-ray energies, 6.5, 7.1, and 16 keV. The ratio I_{211}/I_{310} shows a more rapid rate of decrease, at least initially, for the data obtained at 16 and 7.1 keV compared to that for 6.5 keV (Mn edge, where the Mn is suppressed). This indicates that Mn ions in the (211) planes are being replaced by Fe ions.

Figure 6, the positions of the (110), (200), (220), (310), (400), (330), and (420) peaks do not change with Fe doping; however, the (211), (301), and (411) peaks shift to lower 2θ values. In
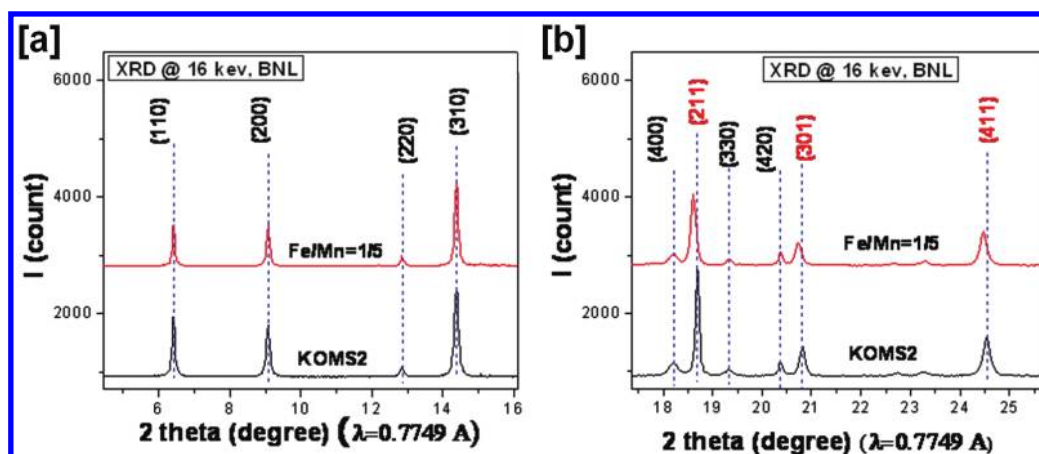
Figure 6. Detailed XRD scans obtained for undoped KOMS-2 and Fe-KOMS-2, Fe/Mn = 1/5 at 16 keV over the ranges (a) $6° \leq 2\theta \leq 16°$ and (b) $18° \leq 2\theta \leq 25°$. In general, the results shown indicate that the ($hk1$) peaks shift to lower 2θ values, but the ($hk0$) peaks do not. This behavior suggests that the Fe is doped into the KOMS-2 cryptomelane structure and, furthermore, results in a lattice expansion along the c axis, parallel to the tunnels.

general, the results shown in Figure 6a and 6b indicate that the ($hk1$) peaks shift but the ($hk0$) peaks do not. This behavior provides additional evidence that the Fe is doped into the KOMS-2 cryptomelane structure and, furthermore, results in a lattice expansion along the c axis, parallel to the tunnels.

D. Extended X-ray Absorption Fine Structure Spectroscopy. In order to investigate the local Fe atomic environment, EXAFS measurements of the Fe K-edge for Fe-KOMS-2 (Fe/Mn = 1/10, 1/5, and 1/3) were done. In addition, the EXAFS of the Mn K-edge for undoped KOMS-2 and Fe K-edge for α-Fe$_2$O$_3$ (hematite) were obtained in order to provide reference models for the fitting procedure. Analysis of EXAFS data involved the transformation of raw data to k space and then back to r space, along with a fitting that involves structural parameters such as the coordination number (CN), the near neighbor distances (R), and mean squared disorder parameters (σ^2). The procedural details and typical plots are provided elsewhere.[12] For undoped KOMS-2 and Fe-KOMS-2, the tetragonal cryptomelane (space group $I4/m$) was used. Figure 7a shows the combined raw data in r space for α-Fe$_2$O$_3$, undoped KOMS-2, as well as Fe-KOMS-2 (Fe/Mn = 1/10, 1/5 and 1/3). Figure 7a shows the combined raw EXAFS data in r space for the analyzed samples. Figure 7b–f shows the r-space fittings and raw data for undoped KOMS-2, Fe-KOMS-2 (Fe/Mn = 1/10, 1/5 and 1/3), and α-Fe$_2$O$_3$, respectively. Additionally, Table 2 summarizes the best fit parameters from the EXAFS for undoped KOMS-2, Fe-KOMS-2 (Fe/Mn = 1/10, 1/5, and 1/3), and α-Fe$_2$O$_3$. As discussed below, reasonable fits to the EXAFS data are obtained using a model based on the cryptomelane KOMS-2 structure and not a model based on the α-Fe$_2$O$_3$ structure. On the basis of the local Fe environment information obtained from EXAFS (summarized in Table 2), the vast majority of the Fe atoms are doped into the cryptomelane KOMS-2 structure; the small amount of second phase γ-Fe$_2$O$_3$ is not detectable in the EXAFS.

E. Mössbauer Spectroscopy. Mössbauer spectra were obtained from the Fe-KOMS-2 samples for selected Fe-doping levels and temperatures. If a (single site) Fe atom is in a magnetically ordered state, the Mössbauer spectrum is characterized by the sextet line structure while the paramagnetic state has either a single line or a quadrupole-split doublet. An excellent review of the experimental techniques and data analysis for Mössbauer

experiments is given by Chen and Yang.[13] As expected, the spectrum obtained from undoped KOMS-2 showed no trace of Fe. For reference, a spectrum was obtained from α-Fe$_2$O$_3$ (hematite) at room temperature, 293 K (see Figure 8a). From the spectrum shown in Figure 8a, values were obtained for the hyperfine field H_{hf} = 514 kOe and quadrupole shift 4ε = 0.42 mm/s, which are consistent with the literature values for α-Fe$_2$O$_3$ (hematite).[14] In addition, the α-Fe$_2$O$_3$ sample was used as a reference for determining the isomer shifts in the Fe-KOMS-2 samples. Figure 8b and 8c shows the Mössbauer spectra for the Fe-KOMS-2 sample with Fe/Mn = 1/10 obtained at 293 and 4.2 K, respectively. From a fitting of the quadrupole-split doublet line structure in Figure 8b, room-temperature (293 K) values were obtained for the quadrupole splitting ΔQ = 0.44 mm/s and isomer shift IS = +0.17 mm/s. From a fitting of the sextet line structure in Figure 8c, low-temperature (4.2 K) values were obtained for the hyperfine field H_{hf} = 461 kOe, isomer shift IS = +0.39 mm/s, and quadrupole shift $4\varepsilon \approx 0$. As discussed below, these results indicate that Fe is present as Fe^{3+} in octahedral environments similar to Mn in MnO$_6$ building blocks of KOMS-2. Figure 8d shows the spectrum obtained from Fe-KOMS-2, Fe/Mn = 1/2, at 50 K. The spectrum shows a combination of both the sextet line structure and the quadrupole-split doublet, i.e., approximately one-half of the Fe appears magnetically ordered, while one-half of the Fe appears paramagnetic. This result is consistent with the magnetic measurements presented below from which a broad magnetic transition between 50 and 100 K was identified. This transition is associated with the Fe-doped cryptomelane KOMS-2 structure and not an Fe oxide impurity such as γ-Fe$_2$O$_3$.

F. Magnetization Measurements. The magnetic properties of the Fe-KOMS-2 materials were characterized by a combination of SQUID and VSM magnetometry. Magnetic hysteresis loops were obtained for all of the Fe-KOMS-2 samples (Fe/Mn = 1/20, 1/10, 1/5, 1/3, and 1/2) for selected temperatures 10 K $\leq$ $T \leq$ 350 K. Figure 9 shows a representative set of the hysteresis loops for (a) three Fe-doping levels, Fe/Mn = 1/10, 1/5, and 1/2, at 300 K and (b) three temperatures, 10, 100, and 300 K, for Fe/Mn = 1/5. As can be seen in Figure 9a, the Fe doping has introduced a ferromagnetic contribution at 300 K, far above the magnetic transition at ~50 K. As discussed below, this is attributed to a small amount of γ-Fe$_2$O$_3$ and not the vast majority of

21614

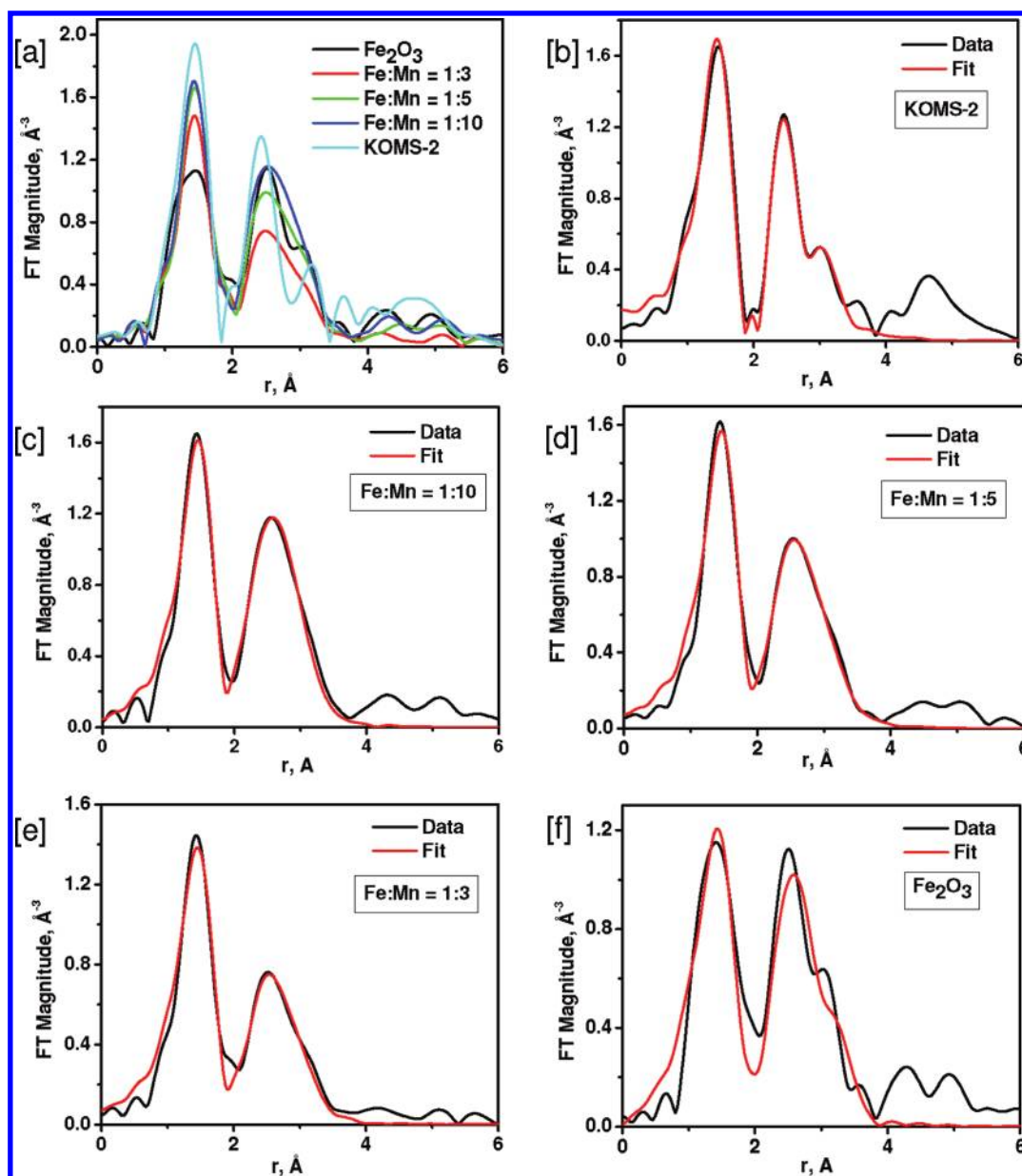dx.doi.org/10.1021/jp206046k |*J. Phys. Chem. C* 2011, 115, 21610–21619

Figure 7. Raw EXAFS data in *R* space (a), and fitting of EXAFS data using the tetragonal cryptomelane model (space group *I4/m*) for (b) undoped KOMS-2, (c) Fe/Mn = 1/10 Fe,KOMS-2, (d) Fe/Mn = 1/5 Fe,KOMS-2, (e) Fe/Mn = 1/3 Fe,KOMS-2, and (f) Fe_2O_3 (hematite) standard. Black lines: Mn K-edge data.

the Fe atoms which are substituted for Mn in the cryptomelane KOMS-2 structure. This is an example of how sensitive magnetic measurements are to even minute quantities of magnetic impurities. The γ-Fe_2O_3 second phase was not detected with the other characterization methods used in this work except for a very small signature using anomalous XRD at the Mn edge. The ferromagnetic contribution of the γ-Fe_2O_3 second phase clearly increases with the Fe-doping level. Although the magnetic results are contaminated by the impurity phase, some useful magnetic information is still obtainable from the magnetization curves for Fe/Mn $\leq$ 1/5. Figure 9a and 9b shows curves that have linear regions for $|H| \geq 10$ kOe and $T \geq 100$ K. The slopes of the linear regions yield values for the magnetic susceptibility $\chi(T)$ which are representative of the magnetic behavior for the Fe-doped cryptomelane KOMS-2 structure. The *y* intercepts yield values for the

saturation magnetization $\sigma(T)$, which are representative of the impurity phase. To explore the applicability of the Curie–Weiss law, $\chi(T)$ is expressed as

$$\chi(T) = C/(T - \Theta) + \chi_o \qquad (1)$$

where *C* is the Curie–Weiss constant, Θ is the Curie–Weiss temperature, and χ_o represents any temperature-independent contribution(s) to the magnetic susceptibility, such as diamagnetism of the ionic cores. The diamagnetic contribution of the sample holder was measured separately and subtracted. Figure 10a shows a Curie–Weiss plot of $1/[\chi(T) - \chi_o]$ versus the temperature *T* for Fe-KOMS-2, Fe/Mn = 1/10. For comparison, the Curie–Weiss plot obtained previously for the host KOMS-2 material is included.[15] By both calculation and fitting, χ_o was neg-

21615

dx.doi.org/10.1021/jp206046k |*J. Phys. Chem. C* 2011, 115, 21610–21619

Table 2. EXAFS Data-Fitting Results

| sample	KOMS-2	Fe-KOMS-2 with Fe/Mn			Fe$_2$O$_3$
		1/10	1/5	1/3	
CN$_{Fe(Mn)-O}$	6	6	6	6	6
CN$_{Fe(Mn)-M1}$	4	4	4	4	4
CN$_{Fe(Mn)-M2}$	4	4.9 (2.9)	3.3 (2.2)	1.9 (2.0)	3
CN$_{Fe(Mn)-M3}$					6
R$_{Fe(Mn)-O}$ (Å)	1.902 (8)	1.970 (16)	1.988 (14)	1.977 (15)	2.000 (26)
R$_{Fe(Mn)-M1}$ (Å)	2.886 (10)	2.941 (15)	2.972 (14)	2.993 (15)	2.961 (21)
R$_{Fe(Mn)-M2}$ (Å)	3.437 (15)	3.441 (20)	3.488 (19)	3.492 (24)	3.386 (41)
R$_{Fe(Mn)-M3}$ (Å)					3.708 (41)
$\sigma^2_{Fe(Mn)-O}$ (Å^2)	0.0042 (11)	0.0075 (13)	0.0082 (12)	0.0105 (12)	0.0127 (25)
$\sigma^2_{Fe(Mn)-M1}$ (Å^2)	0.0038 (11)	0.0051 (16)	0.0053 (15)	0.0081 (19)	0.0053 (12)
$\sigma^2_{Fe(Mn)-M2}$ (Å^2)	0.0048 (17)	0.0051 (54)	0.0035 (63)	0.0033 (94)	0.0053 (12)
$\sigma^2_{Fe(Mn)-M3}$ (Å^2)					0.0146 (87)
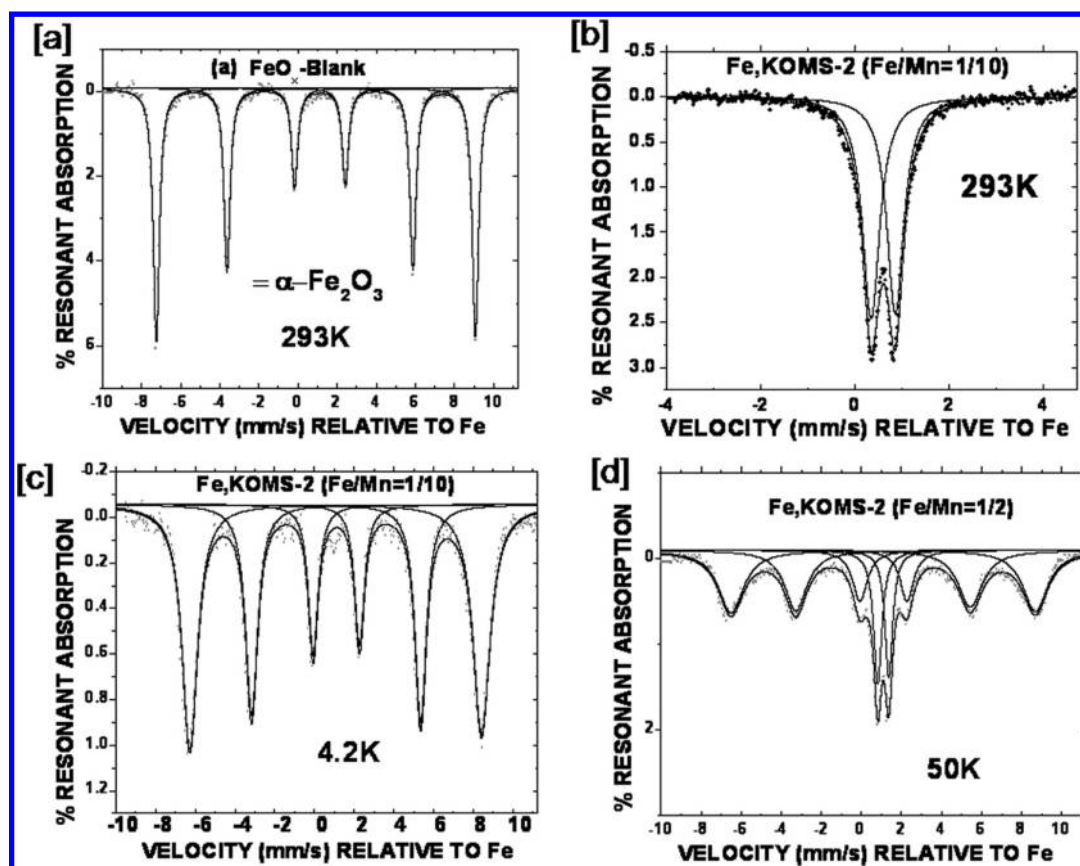
Figure 8. Representative Mössbauer spectra: (a) α-Fe$_2$O$_3$ (hematite) reference sample at 293 K, (b) Fe-KOMS-2 (Fe/Mn = 1/10) at 293 K, (c) Fe-KOMS-2 (Fe/Mn = 1/10) at 4.2 K, and (d) Fe-KOMS-2 (Fe/Mn = 1/2) at 50 K. The doped Fe is present as Fe^{3+} in an octahedral environment similar to Mn^{3+}/Mn^{4+} in the MnO$_6$ building blocks of the cryptomelane KOMS-2 host structure.

ligible.[16] As shown in Figure 10, a reasonable fit to the Curie—Weiss law is obtained for 125 K $\leq T \leq$ 350 K, as indicated by the linear behavior. Although the linear fit was not as good as that for the host KOMS-2 sample, a value of C = 39.0 g/emu-K was obtained from the slope (1/C) and Θ = −460 K from the intercept. Using

$$C = n\mu_{eff}^2/3k_B \qquad (2)$$

where n is the concentration of the magnetic ions, μ_{eff} is the effective magnetic moment, and k_B is the Boltzmann constant, a value of μ_{eff} = 4.4 μ_B is obtained for the combined magnetic moment of mixed-valent Mn (Mn^{3+} and Mn^{4+}) and Fe^{3+}. For the calculation, the formula K$_{0.16}$(Fe$_{0.10}$Mn$_{0.92}$)O$_2$ was used. See Table 1.

Figure 10b shows the "saturation magnetization" $\sigma(T)$ versus temperature for Fe-KOMS-2, Fe/Mn = 1/10 . The true saturation magnetization $\sigma(0)$ = 0.50 emu/g for the sample is

21616

dx.doi.org/10.1021/jp206046k |J. Phys. Chem. C 2011, 115, 21610–21619
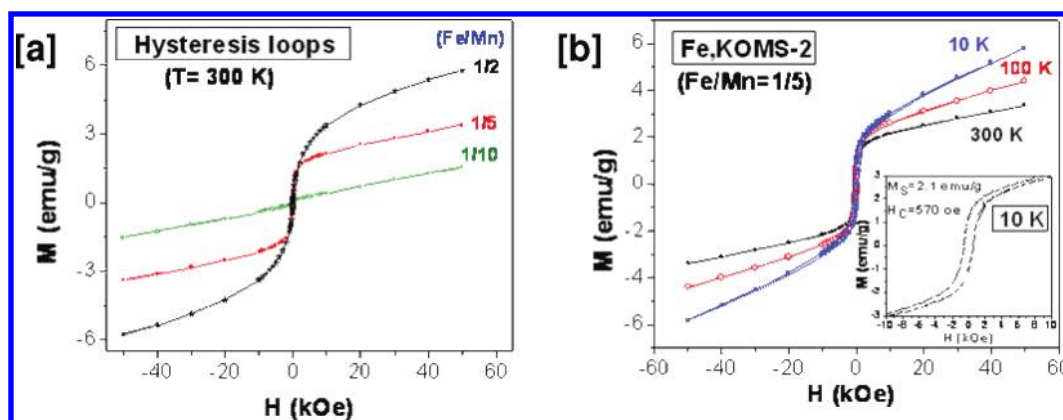
Figure 9. Representative magnetic hysteresis loops: (a) Fe-KOMS-2 for three Fe-doping levels, Fe/Mn = 1/10, 1/5, and 1/2, at 300 K and (b) at three temperatures 10, 100, and 300 K for Fe-KOMS-2 (Fe/Mn = 1/5). The magnetic contribution of the γ-Fe$_2$O$_3$ second phase is clearly apparent; however, magnetic susceptibility values characteristic of the Fe-KOMS-2 materials can be extracted from the linear regions of the hysteresis curves.
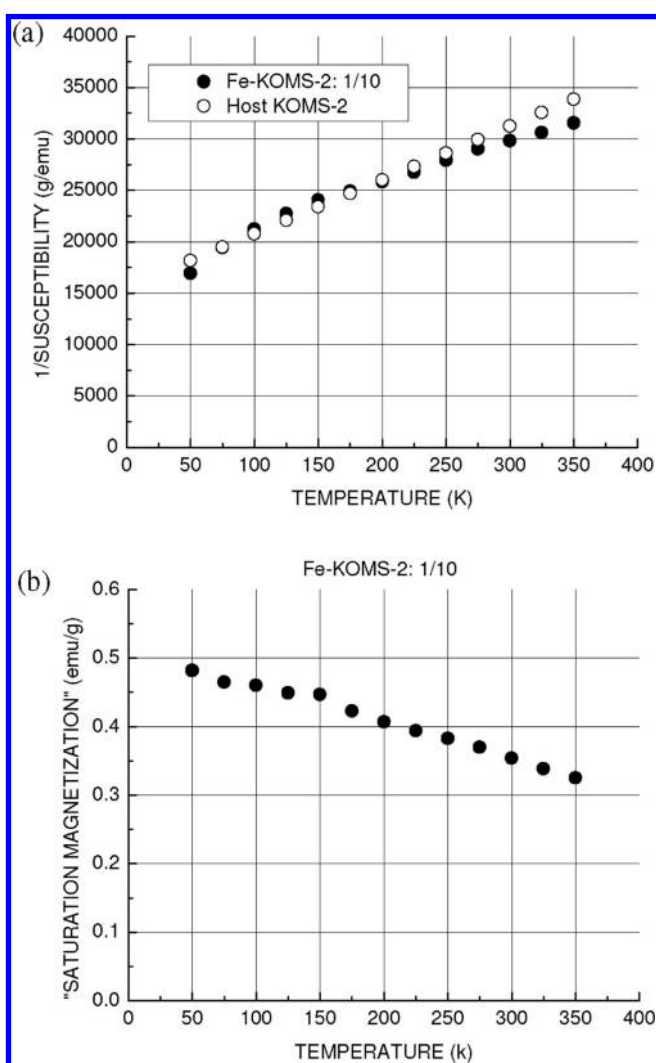

Figure 10. (a) Curie–Weiss plot for (●) Fe-KOMS-2 (Fe/Mn = 1/10) and (○) host KOMS-2 from ref 12. A reasonable fit to the Curie–Weiss law is obtained over the range 125 K ≤ T ≤ 350 K for the Fe-KOMS-2, Fe/Mn = 1/10, sample as indicated by the linear behavior. This fit yields a value of μ_{eff} = 4.4 μ_B from the slope and Θ = −460 K from the intercept. (b) "Saturation magnetization" $\sigma(T)$ versus temperasture T for the Fe-KOMS-2 (Fe/Mn = 1/10) sample. Extrapolation to T = 0 yields a value of $\sigma(T)$ = 0.50 emu/g and an estimate of 0.6 wt % for the γ-Fe$_2$O$_3$ impurity phase.
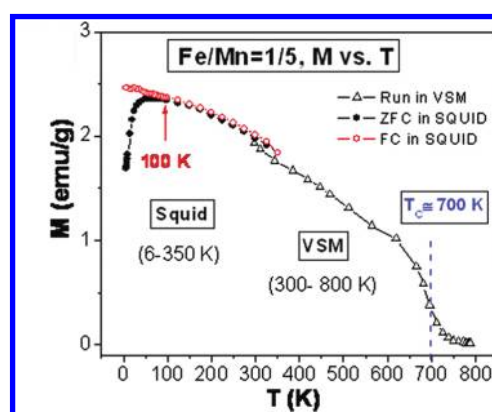

Figure 11. Zero-field-cooled (ZFC) and field-cooled (FC) magnetization curves measured for the Fe-KOMS-2 (Fe/Mn = 1/5) sample in a magnetic field H = 1.0 kOe using a combination of SQUID and VSM measurements. The ZFC and FC curves slowly diverge at ∼100 K with the ZFC curve having a maximum at ∼50 K. This behavior indicates a broad ferromagnetic transition between 50 and 100 K and is attributed to the Mn/Fe moments in the cryptomelane KOMS-2 structure. The magnetic transition at ∼700 K is attributed to transformation of the γ-Fe$_2$O$_3$ impurity phase into α-Fe$_2$O$_3$.

obtained by extrapolation to T = 0. Using the known saturation magnetization $\sigma(0)$ = 80−85 emu/g for (bulk) γ-Fe$_2$O$_3$, the impurity content for F-KOMS-2, Fe/Mn = 1/10, is estimated to be 0.6 wt % of the sample.[17] This means that 7% of the doped Fe atoms are in the impurity.

Figure 11 shows the zero-field-cooled (ZFC) and field-cooled (FC) magnetization curves measured for Fe-KOMS-2, Fe/Mn = 1/5, in a magnetic field H = 1.0 kOe. The measurements were obtained over the temperature range 6.0 K ≤ T ≤ 350 K using the SQUID and overlapping temperature range 300 K ≤ T ≤ 800 K using the VSM. The ZFC and FC curves slowly diverge at ∼100 K with the ZFC curve having a maximum at ∼50 K. This behavior indicates a broad ferromagnetic transition between 50 and 100 K and is attributed to the Mn/Fe moments in the cryptomelane KOMS-2 structure. The magnetic transition ∼700 K is attributed to a phase transition from the γ-Fe$_2$O$_3$ impurity phase to α-Fe$_2$O$_3$.[18] The γ-Fe$_2$O$_3$ second phase, which has a spinel-related structure, is strongly ferrimagnetic, while α- Fe$_2$O$_3$ is weakly paramagnetic.

IV. DISCUSSION AND CONCLUSIONS

This work presents a detailed characterization of the Fe-doped KOMS-2 system over a wide range of doping levels $0 \leq$ Fe/Mn $\leq 1/2$ using a variety of experimental techniques. Using conventional Cu Kα XRD, each sample could be indexed on the tetragonal $I4/m$ cryptomelane structure for Fe/Mn $\leq 1/2$; the elemental composition for each sample was established using ICP-AES.

The morphology and microstructure of the materials was examined using a combination of SEM and TEM images. Upon Fe doping, the images revealed that the morphology changed from nanoneedle to nanorod while maintaining the KOMS-2 cryptomelane structure. Since both KOMS-2 and Fe-KOMS-2 samples were prepared by similar methods and have the same cryptomelane structure, the changes of morphology after Fe doping suggest that Fe may enter the lattice of KOMS-2 resulting in a different particle growth behavior than for undoped KOMS-2. For the longer ultrasonic pretreatment times (10−30 min) a few regions in the TEM images showed small particles. The small particles may be due to the breaking of some of the nanorods. As can be seen in the SEM images (Figure 2b), some of the rods intergrew together; the intergrowth points may be the weak sections that are broken during the ultrasonic pretreatment.

Analysis of the thermal stability by TGA showed that the structural collapse temperature increases with Fe doping. All of the samples only show significant weight loss for temperatures greater than 600 °C, which is attributed to release of oxygen as seen in other OMS materials.[11] The increased thermal stability with increasing Fe-doping levels also suggests that Fe is doped into the KOMS-2 cryptomelane structure affecting the bonding strength of the atoms.

Anomalous XRD was used to differentiate between the diffraction contributions from the Fe and Mn. The intensity of an XRD peak is determined by the summation of diffraction contributions from each element in the crystal structure, e.g., for KOMS-2, there are contributions from K, Mn, and O. The diffraction contribution from each element is proportional to the atomic number of that element. For Fe-KOMS-2, the difference in atomic number between Fe and Mn is only one, and it is difficult to differentiate between the diffraction contributions from Fe and Mn using a conventional Cu Kα X-ray source. Therefore, it is difficult to determine if Fe replaces Mn in the KMOS-2 structure using Cu Kα radiation. However, if the X-ray energy is moved to the absorption edge of one element, such as Mn, then the diffraction contribution from Mn is minimized and the diffraction contrast between Fe and Mn will be enhanced. By measuring the peak intensity for the (211) reflection relative to the (310) reflection, Mn ions in the (211) planes are being replaced by Fe ions. Furthermore, detailed XRD scans over selected 2θ regions indicated that the (hk1) shift downward but the (hk0) peaks do not. This behavior provides additional evidence that the Fe is doped into the KOMS-2 cryptomelane structure and results in a lattice expansion along the c axis, parallel to the tunnels. The Mn^{3+} ions in KOMS-2 tend to be in the low-spin state as previously shown.[15] Assuming a coordination number of 6, the Shannon crystal radii for Fe^{3+} in a high-spin state is 0.785 Å, Mn^{4+} is 0.67 Å, and Mn^{3+} is 0.72 Å.[19] This is consistent with the observed lattice expansion after Fe doping. Finally, a structure refinement, using the space group $I4/m$, was carried for KOMS-2 and Fe-KOMS-2, Fe/Mn = 1/5. At the Fe edge (7.1 keV) for KOMS-2, the cell parameters are $a = b = 9.85078$ Å and $c = 2.86374$ Å, and for Fe-KOMS-2 the cell

parameters are $a = b = 9.845536$ Å and $c = 2.87535$ Å. The cell expansion along the c axis agrees with the qualitative observation from peak shifts. However, the Fe contribution to the XRD pattern is more visible at the Mn edge compared to the Fe edge. At the Fe edge, Fe-KOMS-2, Fe/Mn = 1/5, shows an XRD pattern with only a single KOMS-2 phase. However, at the Mn edge, the Fe contribution is more pronounced and two small second-phase peaks were observed at $2\theta \approx 36°$ and 45°. As verified by magnetic measurements, the second phase is attributed to γ-Fe_2O_3 (maghemite) and the estimated amount is 1.5 wt % for the Fe/Mn = 1/5 sample.

Information concerning the local Fe atomic environment in Fe-doped KOMS-2 was obtained by measuring the Fe K-edge EXAFS for Fe-KOMS-2 (Fe/Mn = 1/10, 1/5, and 1/3) as shown in Figure 7. In addition, the Mn K-edge EXAFS for undoped KOMS-2 and Fe K-edge EXAFS for α-Fe_2O_3 (hematite) were obtained for reference additionally shown in Figure 7. Table 2 summarizes the best-fit values for the coordination number (CN), the near neighbor distances (R), and mean squared disorder parameter (σ^2) parameters from the EXAFS for undoped KOMS-2, Fe-KOMS-2 (Fe/Mn = 1/10, 1/5, and 1/3), and α-Fe_2O_3 for fits of the data in r space. Crystallographically, the KOMS-2 host material and Fe_2O_3 samples are characterized by coordination numbers of 6 and 4 for the first two shells (M−O and M−M1, respectively). Therefore, these numbers were fixed in the various fits as they are not expected to change between the two models of the local atomic structure for Fe. The more distant third metal−metal coordination shell (M−M2) has different occupancies for these two structures, i.e., the coordination numbers for KOMS-2 and α-Fe_2O_3 structures are 4 and 3, respectively. However, the numbers are close and not easily distinguished by EXAFS analysis, particularly for such a distant shell ($\sim$3.4 Å). Thus, determination of the Fe dopant environment based on coordination numbers of the first three shells only is extremely difficult. However, in α-Fe_2O_3 there is another Fe−Fe contribution (denoted here as M-M3), which is 4-fold degenerate and has a near neighbor distance of 3.71 Å. Since there is no such contribution in the cryptomelane KOMS-2 structure, its presence or absence in the Fe-KOMS-2 materials can be used as a signature to differentiate between the two models for Fe incorporation in the KOMS-2 host. From the best-fit parameters listed in Table 2, with the increase of Fe doping from Fe/Mn = 0 (undoped KOMS-2) to Fe/Mn = 1/10 and beyond, the R(M−O) bond distance increases from 1.90 to 1.98 Å. The longer M−O near neighbor distance in the Fe-doped materials compared to that for undoped KOMS-2 is consistent with the results from anomalous XRD and attributed to the larger size of Fe^{3+} compared to Mn^{3+}/Mn^{4+}. Furthermore, the Fe-doped materials are characterized by R(M−M2) near neighbor distances that are much closer to that for the host KOMS-2 structure than the α-Fe_2O_3 structure. In summary, reasonable fits to the EXAFS data are obtained using a model based on the tetragonal cryptomelane KOMS-2 structure ($I4/m$) and not a model based on the α-Fe_2O_3 structure. The principal evidence ruling out the latter is the absence of an M−M3 contribution in the fits. On the basis of the local Fe environment information obtained from EXAFS (results presented in Table 2), the vast majority of the Fe atoms are doped into the cryptomelane KOMS-2 structure; the small amount of second-phase γ-Fe_2O_3 is not detectable.

Mössbauer spectra were obtained at various temperatures for selected Fe-KOMS-2 samples. The results for the Fe/Mn = 1/10 sample are representative in that (1) at low temperature (4.2 K) the spectrum is characterized by a sextet line structure with a

hyperfine field value H_{hf} = 461 kOe, an isomer shift IS = +0.39 mm/s, and a quadrupole shift $4\varepsilon \approx 0$ and (2) at room temperature (293 K) the spectrum is characterized by a quadrupole-split doublet structure with a quadrupole splitting value ΔQ = 0.44 mm/s and an isomer shift = +0.17. The Mössbauer parameters for Fe-KOMS-2, Fe/Mn = 1/10, are reminiscent of those observed previously for ferric oxyhydroxide (FeOOH), which is reasonable since the Fe^{3+} environment is quite similar in the two systems.[20] However, no evidence was observed for the presence of FeOOH in the Fe-KOMS-2 samples from XRD, TEM, and EXAFS. These results indicate that the Fe is present as Fe^{3+} in octahedral environments similar to Mn in MnO_6 building blocks of KOMS-2. In addition, the spectrum obtained from Fe-KOMS-2, Fe/Mn = 1/2, at 50 K showed a combination of both the sextet line structure and the quadrupole-split doublet structure. This result is consistent with the magnetic measurements presented below from which a broad magnetic transition between 50 and 100 K was identified. This transition is associated with the Fe-doped cryptomelane KOMS-2 structure and not an Fe oxide impurity such as γ-Fe_2O_3.

The magnetic properties of the Fe-KOMS-2 materials were characterized by a combination of SQUID and VSM magnetometry. Measurements of the magnetization as a function of the magnetic field were made for all of the Fe-KOMS-2 at selected temperatures 10 K $\leq T \leq$ 350 K. Each magnetization curve consisted of two contributions: (1) a linear contribution from which a paramagnetic susceptibility value $\chi(T)$ was calculated that characterized the Fe-doped host KOMS-2 and (2) a contribution that saturated $\sigma(T)$ which was attributed to the trace amount of second-phase γ-Fe_2O_3 impurity. The $\chi(T)$ values for the Fe/Mn = 1/10 sample provided a reasonable fit to the Curie–Weiss law, yielding a value of Θ = −460 K for the Curie–Weiss temperature and a value of μ_{eff} = 4.4 μ_B for the effective magnetic moment of mixed-valent Mn (Mn^{3+} and Mn^{4+}) and Fe^{3+}. Previous magnetic measurements have been carried out by Shen et al.[15] on undoped KOMS-2 prepared by the sol–gel combustion method as well as other manganese oxide systems. By fitting the magnetic susceptibility data for KOMS-2 to the Curie–Weiss law over the temperature range 100 K $\leq T \leq$ 350 K, they were able to calculate a magnetic moment value of 3.74 μ_B for the mixed-valent Mn ions and, therefore, the average oxidation state (3.88). They also obtain a negative value for the Curie–Weiss temperature of −297 K which indicates strong antiferromagnetic interactions between the Mn moments. For Fe-KOMS-2, Fe/Mn = 1/10 reported here, the magnetic moment value for Mn^{3+}/Mn^{4+} + Fe^{3+} is larger (4.4 μ_B), indicating the substituted Fe^{3+} is in the high-spin state. For reference, the low-spin, intermediate-spin, and high-spin values for Fe^{3+} are 1.73, 3.87, and 5.92 μ_B, respectively. Finally, in the earlier work by Shen et al.,[15] they report a very weak magnetic feature at ~225 K and the onset of weak ferromagnetism at ~50 K. Sato et al.[21] carried out a combination of magnetic and transport measurements on single-crystal samples of KOMS-2. They observed three magnetic transitions with decreasing temperature: (1) a very weak feature which varied between 180 and 250 K and depended on the sample preparation conditions, (2) the onset of weak ferromagnetism at 52 K, and (3) the disappearance of the weak ferromagnetism at 20 K. Using the previous results on the host KOMS-2 material reported by both Shen et al.[15] and Sato et al.,[21] the broad magnetic transition 50−100 K reported here is clearly attributed to the Mn and Fe moments in the cryptomelane KOMS-2 structure and not the γ-Fe_2O_3 impurity.

A magnetic transition associated with the impurity was observed at ~700 K.

■ AUTHOR INFORMATION

Corresponding Author
*E-mail: steven.suib@uconn.edu.

■ REFERENCES

(1) Shen, Y. F.; Zerger, R. P.; DeGuzman, R. N.; Suib, S. L.; McCurdy, L.; Potter, D. I.; O'Young, C. L. *Science* **1993**, *260*, 511.

(2) Feng, Q.; Kanoh, H.; Miyai, Y.; Ooi, K. *Chem. Mater.* **1995**, *7*, 148.

(3) Suib, S. L. *Acc. Chem. Res.* **2008**, *41*, 479.

(4) Suib, S. L. *Curr. Opin. Solid State Mater. Sci.* **1998**, *3*, 63.

(5) http://chemistry.uconn.edu/SuibGroup/manganeseoxides.htm.

(6) Ramsdell, A. *Am. Mineral.* **1942**, *27*, 611.

(7) Chen, X.; Shen, Y. F.; Suib, S. L.; O'Young, C. L. *Chem. Mater.* **2002**, *14*, 940.

(8) Kumar, R.; Sithambaram, S.; Suib, S. L. *J. Catal.* **2009**, *262*, 304.

(9) King'ondu, C. K.; Opembe, N.; Chen, C. H.; Ngala, K.; Huang, H.; Iyer, A.; Garces, H. F.; Suib, S. L. *Adv. Funct. Mater.* **2011**, *21*, 312.

(10) Liu, J.; Son, Y. C.; Cai, J.; Shen, X. F.; Suib, S. L.; Aindow, M. *Chem. Mater.* **2004**, *16*, 276.

(11) DeGuzman, R. N.; Shen, Y. F.; Neth, E. J.; Suib, S. L.; O'Young, C. L.; Levine, S.; Newsam, J. M. *Chem. Mater.* **1994**, *6*, 815.

(12) Koningsberger, D. C.; Prins, R. *X-ray Absorption, Principles, Applications, Techniques of EXAFS, SEXAFS, and XANES*; Wiley: New York, 1988.

(13) Chen, Y. L.; Yang, D. P. *Mössbauer Effect in Lattice Dynamics*; Wiley-VCH: Weinheim, Germany, 2007.

(14) Kundig, W.; Bommel, H.; Constabaris, G.; Lindquist, R. H. *Phys. Rev.* **1966**, *142*, 327.

(15) Shen, X. F.; Ding, Y. S.; Liu, J.; Han, Z. H.; Budnick, J. I.; Hines, W. A.; Suib, S. L. *J. Am. Chem. Soc.* **2005**, *127*, 6166.

(16) Selwood, P., *Magnetochemistry*; Interscience: New York, 1956; p 78.

(17) Dutta, P.; Manivannan, A.; Seehra, M. S.; Shah, N.; Hoffman, G. P. *Phys. Rev. B* **2004**, *70*, 174428.

(18) Helgason, Ö.; Greneche, J.-M.; Berry, F. J.; Mosselmans, F. J. *Phys.: Condens. Matter* **2003**, *15*, 2907.

(19) Shannon, R. *Acta Crystallogr.* **1976**, *A32*, 751.

(20) Vandenberghe, R. E.; De Grave, E.; Landuydt, C.; Bowen, L. H. *Hyperfine Interact.* **1990**, *53*, 175.

(21) Sato, H.; Enoki, T.; Yamaura, J. I.; Yamamoto, N. *Phys. Rev. B* **1999**, *59*, 12836.